PCCP

Momentum-dependent band spin splitting in semiconducting MnO_2: A density functional calculation

Journal:	*Physical Chemistry Chemical Physics*
Manuscript ID	CP-ART-12-2015-007806.R2
Article Type:	Paper
Date Submitted by the Author:	14-Apr-2016

Complete List of Authors:	Noda, Yusuke; RIKEN Innovation Center, Nakamura Laboratory; Yokohama National University, Department of Physics, Graduate School of Engineering Ohno, Kaoru; Yokohama National University, Department of Physics, Graduate School of Engineering Nakamura, Shinichiro; RIKEN Innovation Center, Nakamura Laboratory

Momentum-dependent band spin splitting in semiconducting MnO_2: A density functional calculation

Yusuke Noda,[1,2,*] Kaoru Ohno,[2] and Shinichiro Nakamura[1]

[1]*RIKEN Innovation Center, Nakamura Laboratory, 2-1 Hirosawa, Wako, Saitama 351-0198, Japan*

[2]*Department of Physics, Graduate School of Engineering, Yokohama National University, 79-5 Tokiwadai, Hodogaya, Yokohama 240-8501, Japan*

Abstract

Recently, manganese-oxide compounds have attracted considerable attention, in particular, as a candidate of materials exhibiting a photochemical water-splitting reaction. Here, we investigate electronic states of pristine manganese dioxides (MnO_2) at different crystal phases using spin-polarized density functional theory (DFT) with Hubbard U correction. Geometrical structures and band dispersions of α-, β-, δ-, and λ-MnO_2 crystals with collinear magnetic [ferromagnetic (FM) and antiferromagnetic (AFM)] orders are discussed in detail. We reveal that penalty energies that arise by violating the Goodenough-Kanamori rule are important and the origin of the magnetic interactions of the MnO_2 crystals is governed by the superexchange interactions of Mn–O–Mn groups. In addition, it is found that momentum-dependent band spin splitting occurs in the AFM α-, β-, and δ-MnO_2 crystals while no spin splitting occurs in the AFM λ-MnO_2 crystal. Our results show that spin-split band dispersions stem from the different orientations of Mn-centred oxygen octahedra. Such interesting electronic states of the MnO_2 crystals are unraveled by our discussion on the relationship between the effective (spin-dependent) single-electron potentials and the space-group symmetry operations that map up-spin Mn atoms onto down-spin Mn atoms. This work provides a basis to understand the relationship between the spin-dependent electronic states and the crystallography of manganese oxides. Another relationship to the recent experimental observations of the photochemical oxygen evolution of MnO_2 crystals is also discussed.

PACS numbers: 71.15.Mb, 75.50.Pp

I. INTRODUCTION

Manganese oxides have been synthesized with a wide variety of crystallographic structures[1], and attracted extensive research attentions such as electrode materials for rechargeable lithium-ion batteries[2,3], agents for magnetic resonance imaging[4], and catalysts[5,6] especially for water-splitting reactions. One of the most representative examples of the manganese-oxide catalysis is the oxygen-evolution complex (OEC) in photosystem II (PSII) for natural photosynthesis[7]. The OEC, a manganese-oxide cluster, is a central component of oxygen evolution in the PSII functioning without any bias voltage and only with abundant sunlight energy.

A geometrical structure of the OEC had been unknown for many years. Very recently, Shen's group[8,9] has determined the structure of the OEC, that is a Mn_4CaO_5 cluster, by X-ray diffraction with high resolution of 1.9 and 1.95 Å. Based on the X-ray structures, many researchers have attempted to reveal a reaction mechanism of water oxidation on the OEC[10], however, the details of the oxidation mechanism on a molecular level still remain unclear. The reason for the difficulty lies at least in two aspects. One is from electronic structural point of view; the difficulty exists in the spin state of the catalyst accelerating a reaction that two water molecules (reactants) of singlet spin states produce one oxygen molecule (products) of triplet spin states. The other is from precise geometrical structural point of view; the difficulty lies in the fact that the OEC structure is known only for a dark-stable S_1 state[11–14], although the OEC catalytic cycle consists of at least four states[7,10,15].

When it comes to the oxygen-evolution reaction by water splitting, in most of the artificial electrodes, precious metals such as platinum, ruthenium, and iridium are often indispensable[16,17], owing to their durability. By contrast, in natural photosynthesis, an abundant metal of manganese is used at the heat of the OEC manganese-oxide catalysis. Therefore, for future precious-metal-free artificial photosynthesis, it is crucial to learn the catalytic mechanism of the Mn_4CaO_5 cluster in PSII.

Aiming at the elucidation of this mechanism, many studies are already reported focusing on its molecular properties[7]. In parallel with these molecular quantum chemical studies, we believe it indispensable to investigate the bulk solid catalyst of manganese oxides. It will be natural to presume that the first stage candidate-material of the devices for artificial photosynthesis is consisting of solid state catalysts such as manganese oxides. In fact, there are recent experimental observations of the oxygen evolution of manganese oxides[18–21] and related substances[22–24].

In the present work, we systematically investigate the electronic states of stoichiometric manganese dioxides (MnO_2) using first-principles calculations as a first step toward the investigation of such materials. The aim of this work is to present the explicit spin-dependent band structures of α-, β-, δ-, and λ-MnO_2 crystals with the most probable magnetic orders. The spin-polarized density functional theory (DFT) with Hubbard U correction (DFT+U) is used in our calculations. So far, antiferromagnetic (AFM) α-MnO_2 was investigated by Cockayne *et al.*[25] using DFT+U; β-MnO_2 was investigated by Franchini *et al.*[26] using DFT, DFT+U, and hybrid functional methods; ferromagnetic (FM) δ-MnO_2 was investigated by Kwon *et al.*[27] using DFT (monolayer system was investigated by Sun *et al.*[28] using DFT+U); AFM λ-MnO_2 was investigated by Morgan *et al.*[29] using DFT. However, all these literatures have not shown explicitly or not well explored the details of the spin-dependent band structures. We focus in this study on the spin-dependent band structures of the pure crystalline phases, which would govern an essential property in natural OEC as well as artificial systems for oxygen-evolution reaction.

In particular, a variety of spin-dependent band structures appears in these MnO_2 crystals. The interesting feature is the spin splitting and degeneracy in the band structures, which have never been discussed so far. We will demonstrate that there is a beautiful group-theoretical rule that determines the spin splitting and degeneracy at a given $\boldsymbol{k}$-point in the first Brillouin zone. It is related to the existence of the symmetry operations that map up-spin Mn atoms onto down-spin Mn atoms. Recently, spin splitting and degeneracy have been discussed with much interest in surfaces, edges, or low-dimensional systems in a context of topological insulators[30,31]. However, the mechanism is quite different from the present systems; in our discussion of the MnO_2 systems, it is not necessary to introduce neither the spin-orbit coupling nor the time-reversal symmetry. Instead, it is enough to recognize that AFM α-, β-, and λ-MnO_2 have at least one space-group symmetry that maps every oxygen octahedron surrounding an up-spin Mn atom onto the other oxygen octahedron surrounding a down-spin Mn atom. What we find in this paper is that, if a wave vector $\boldsymbol{k}$ is unchanged under such a symmetry operation, there is a spin degeneracy at this $\boldsymbol{k}$-point. Otherwise, if $\boldsymbol{k}$ is transferred to $\boldsymbol{k}'$ under such a symmetry operation, the up-spin energy levels at the $\boldsymbol{k}$ point coincide with the down-spin energy levels at the $\boldsymbol{k}'$ point, and *vice versa*.

The rest part of this paper is organized as follows. In Chapter Ⅱ, we describe a computational method used in this study. In Chapter Ⅲ, after briefly presenting a general explanation on the interaction between Mn-centred oxygen octahedra, we present the resulting band structures and the density of states (DOS) as well as the unit cell and the first Brillouin zone each for α-, β-, δ-,

and λ-MnO_2. The mechanism of the spin splitting and degeneracy and then a possible relationship of the present results to the catalytic behaviour observed experimentally in MnO_2 crystals[18,19] are discussed in Chapter IV. Finally, Chapter V concludes this paper.

II. COMPUTATIONAL METHOD

In the present study, we use Vienna *ab initio* simulation package (VASP)[32] based on DFT and the projector-augmented-wave (PAW) pseudopotential approach[33,34]. Perdew-Burke-Ernzerhof (PBE) generalized gradient approximation (GGA) functional[35] and Hubbard correction[36] with different U_{eff} (0.00, 3.00, 4.00, or 5.00 eV) are used. The cutoff energy for plane-wave basis is set high enough at 800 eV, and the magnetic moment of each Mn atom is initially set at $\pm$ 3.00 μ_{B} corresponding to Mn(IV). We carry out geometrical optimizations with the unit-cell relaxations. For the $\boldsymbol{k}$-points, we use a Γ-centred grid with $12 \times 12 \times 4$ for α-MnO_2, $8 \times 8 \times 12$ for β-MnO_2, and $12 \times 12 \times 4$ for δ-MnO_2, and a Monkhorst-Pack grid[37] with $6 \times 6 \times 6$ for λ-MnO_2. The tetrahedron method[38] is used for the DOS calculations. All primitive unit cells and conventional unit cells (in the cases of α-MnO_2 and λ-MnO_2) with the most probable magnetic order (see Chapter Ⅱ I) are generated by Phonopy[39]. All symmetry $\boldsymbol{k}$-points and symmetry $\boldsymbol{k}$-lines in the Brillouin zone are determined by Automatic Flow (AFLOW)[40,41].

III. RESULTS

We have to discuss the spin configuration of Mn atoms in the MnO_2 crystals. There are two types of sharings of Mn-centred oxygen octahedra: point and ridge sharings; see Fig. 1. Focusing on any of two adjacent Mn atoms, a preferable spin configuration can be easily identified according to the Goodenough-Kanamori rule[42–44]. It states that superexchange interactions favour AFM when the *d* orbitals of transition metal cations overlap the same *p* orbital of a shared anion as in a linear (180°) Mn–O–Mn group, while they favour FM when the *d* orbitals overlap the same *p* orbital as in a bent (90°) Mn–O–Mn group. After the structural optimization of all MnO_2 crystals studied here, Mn–O–Mn groups at the point sharing are almost linear (about 130°) and those at the ridge sharing are bent (about 100°). Therefore, we find that AFM configuration is favourable in the case of point sharing, whereas FM configuration is favourable in the case of ridge sharing (similar discussion on the relationship between the bond angle and the spin configuration of metal–ligand–

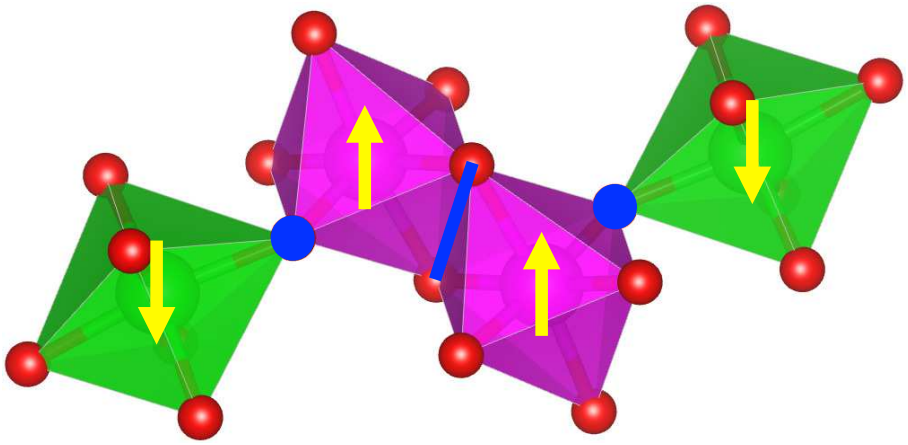

Fig. 1: Spin configuration of Mn atoms in oxygen octahedra. Magenta-, green-, and red-coloured balls denote Mn atoms with up-spin magnetic moment, Mn atoms with down-spin magnetic moment, and O atoms, respectively (the definition is also applied for Figs. 2, 4, 6, 9, and 11). Yellow-coloured arrows denote the spin orientation of each Mn atom. AFM configuration is favourable with the point sharing (blue solid circle), whereas FM configuration is favourable with the ridge sharing (blue solid line).

metal groups was described by P. J. Hay *et al.*[45]). The resulting magnetic moment of each Mn atom remains at ± 3.00 μ_B, which corresponds to Mn(IV).

We have performed density functional calculations with different U_{eff} and compared these results. Table 1 shows the total energy difference between FM and AFM configurations depending on U_{eff} values (the AFM configuration for each crystal phase in the main text of our paper is more stable than any other AFM configurations; see Figs. S1–S4 and Table S1 in Supplementary Information). It is found that the energetic stabilities of the MnO_2 crystals except δ-MnO_2 depend on the strength of Hubbard U correction. Because FM and AFM orders compete in α- and β-MnO_2, AFM is favoured for U_{eff} = 0.00–4.00 eV but FM is favoured for U_{eff} = 5.00 eV as seen in Table 1. According to the discussion in the perspective article authored by H. Xiang *et al.*[46], the strong Hubbard U correction results in the energetic stability of FM systems due to the weak AFM component of the spin exchange interaction. In the case of δ-MnO_2, there is no energy difference between FM and AFM orders. For λ-MnO_2, oxygen octahedra are ridge sharing, and FM should be favoured. Indeed, FM is favoured in our calculations with U_{eff} = 3.00, 4.00, and 5.00 eV. However, AFM is observed experimentally. In our calculation, AFM is favourable when we set U_{eff} = 0.00 eV. Therefore, there is a quite delicate energy competition between the AFM and FM orders

Table 1: Total energy difference $\Delta E^{\rho}_{\rm tot}$ ($\rho = \alpha, \beta, \delta$, and λ) between FM and AFM configurations per MnO_2 unit depending on $U_{\rm eff}$ values. The energy difference is defined as $\Delta E^{\rho}_{\rm tot} = E^{\rho,{\rm FM}}_{\rm tot} - E^{\rho,{\rm AFM}}_{\rm tot}$, where $E^{\rho,{\rm FM}}_{\rm tot}$ and $E^{\rho,{\rm AFM}}_{\rm tot}$ denote the ground-state total energies of the FM and AFM ρ-MnO_2, respectively. The unit of the energy is eV.

$U_{\rm eff}$	α-MnO_2	β-MnO_2	δ-MnO_2	λ-MnO_2
0.00	0.068	0.097	0.000	0.012
3.00	0.009	0.020	−0.001	−0.011
4.00	0.006	0.006	0.000	−0.017
5.00	−0.047	−0.047	0.000	−0.024

in λ-MnO_2, it is difficult to draw any decisive conclusion about the magnetic energy stability. It is commonly known that DFT is a reliable first-principles method to calculate the ground-state total energy but not so reliable for discussing band structures. On the other hand, the DFT+U is considered to be more reliable for the band structures in a sense that it enlarges the band gap that was largely underestimated by standard exchange-correlation functionals (*e.g.* GGA functional). The DFT+U calculations are reviewed in Ref. 47. The typical examples are the magnetic oxides such as MnO and NiO. The usual spin density functionals give correct spin states, but their energy gap is much too small. This is corrected by the introduction of U that increases the gap between the filled and empty 3d states[48]. Therefore, the energy difference might be more reliable for $U_{\rm eff}$ = 0 and the band structures might be more reliable for $U_{\rm eff} > 0$. However, we believe that such an inconsistent use of different $U_{\rm eff}$ values for different purposes is not relevant for current study. More detail energy comparison is left for the future study. In this paper, only the results in the case of $U_{\rm eff}$ = 4.00 eV are adopted. Before taking up the details of our results, it is noteworthy that different $U_{\rm eff}$ does not affect the description of spin splitting and degeneracy in band structures of any MnO_2 crystal (see Figs. S5–S7 in Supplementary Information).

A. α-MnO_2

The α-MnO_2 crystalline phase has a space-group symmetry $I4/m$ (87) with a body-centred tetragonal lattice type 1 (BCT_1, see Fig. 2). The relaxed lattice constants inferred from our geometrical optimization are a = 9.887 Å and c = 2.920 Å (experimental lattice constants[49] are a =

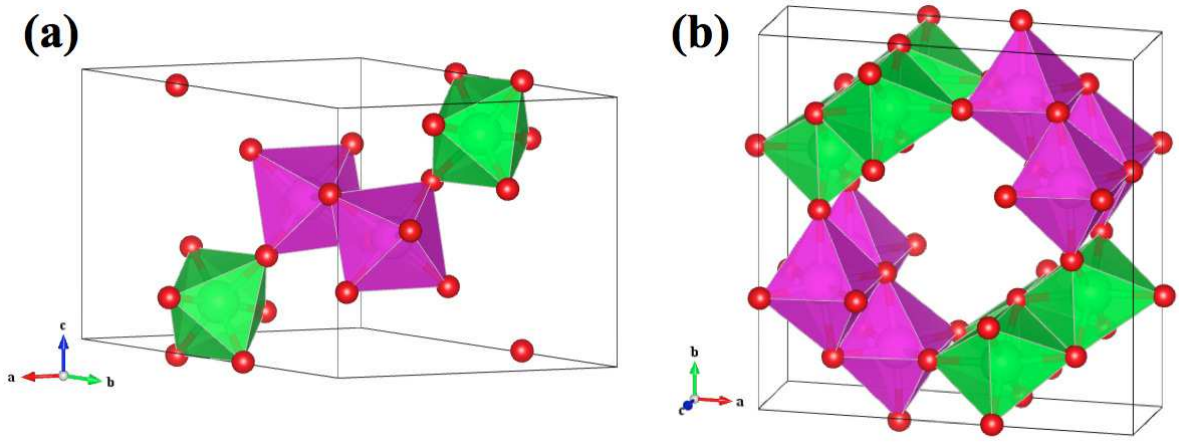

Fig. 2: (a) Primitive and (b) conventional unit cells of AFM α-MnO_2.

9.750 Å and c = 2.861 Å). All the oxygen octahedra in α-MnO_2 are connected to each other by point or ridge sharing like Fig. 1. Therefore, the AFM order is preferable in this case. The Brillouin zone is shown in Fig. 3(a). Comparing to the original figure of the Brillouin zone given in the reference of AFLOW[40], we draw twice a larger number of the symmetry $\boldsymbol{k}$-lines to discuss spin-dependent band structures. For example, the **X** and **X'** points in the Brillouin zone are equivalent in terms of the geometrical symmetry of α-MnO_2. However, the electronic states at the **X** and **X'** points are not equivalent; meanwhile the energy levels of up-spin state at the **X** point and down-spin state at the **X'** point are the same, and *vice versa* (the detail is explained in Chapter IV). The DOS is shown in Fig. 3(b). There is a large contribution of oxygen 2p orbitals to the DOS of the valence bands. In contrast, there is a large contribution of manganese 3d orbital to the DOS of the conduction bands. Our result shows that α-MnO_2 is a semiconductor with an indirect band gap of 1.40 eV [between the **M** point (valence band) and the **X** point (conduction band)]. Its band structures are shown in Figs. 3(c) and (d). Along the symmetry $\mathbf{\Gamma - Z}$ and $\mathbf{Z_1 - M}$ lines, the energy bands of up- and down-spin electrons are completely the same. On the other hand, along the other $\boldsymbol{k}$-lines, the energy bands of up- and down-spin electrons are different. In brief, momentum-dependent band spin splitting occurs in some manner (the mechanism of the spin splitting and degeneracy of this and the following structures will be discussed in Chapter IV).

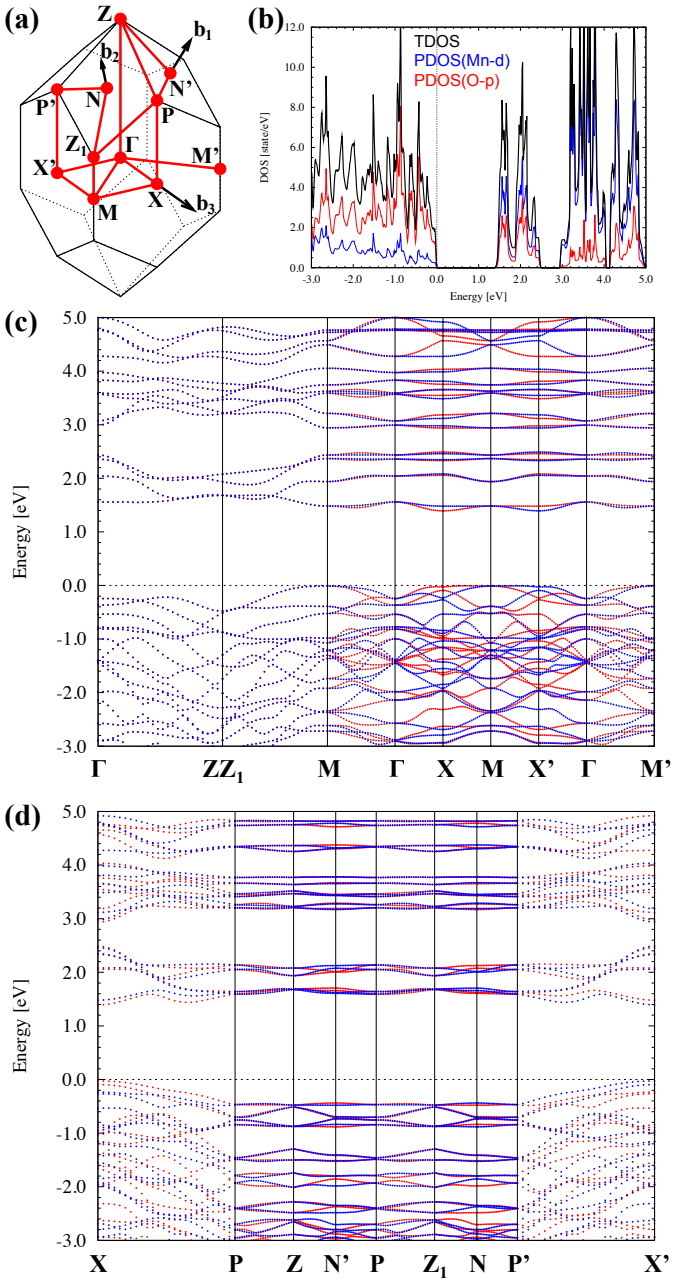

Fig. 3: (a) Brillouin zone of BCT_1 lattice for α-MnO_2. The figure is made by modifying Fig. 5 in the reference of AFLOW[40]. The red circles and lines denote the symmetry $\boldsymbol{k}$-points and $\boldsymbol{k}$-lines. (b) Total DOS (black solid line) and partial DOS of manganese 3*d* and oxygen 2*p* orbitals (blue and red solid lines, respectively) for AFM α-MnO_2. Band structures of AFM α-MnO_2 along (c) the **Γ – Z | Z_1 – M – Γ – X – M–X'–Γ–M'** lines and (d) the **X – P – Z–N'–P – Z_1 – N–P'–X'** lines. Red and blue points denote up- and down-spin energy levels at each $\boldsymbol{k}$-point, respectively. A black dashed line in (b)–(d) is the Fermi level (these definitions are also applied for Figs. 5, 7, 8, and 10).

B. β-MnO_2

The β-MnO_2 crystal has a space-group symmetry $P4_2/mnm$ (136) with a simple tetragonal lattice (TET, see Fig. 4). The relaxed lattice constants from our geometrical optimization are a = 4.450 Å and c = 2.937 Å. All the oxygen octahedra in the structure of β-MnO_2 are connected to each other by point or ridge sharing. Being the same as α-MnO_2, our result indicates that the AFM order is preferable. The Brillouin zone is shown in Fig. 5(a) and the DOS is shown in Fig. 5(b). Similar to the case of α-MnO_2, there is a large contribution of oxygen $2p$ orbitals to the DOS of the valence bands, whereas there is a large contribution of manganese $3d$ orbital to the DOS of the conduction bands. According to our result, β-MnO_2 is a semiconductor with a very small band gap of 0.04 eV (direct band gap at the **Γ** point). This band gap, however, becomes a bit larger ~0.17 eV if we use the experimental lattice constants[50] (a = 4.404 Å and c = 2.876 Å). The band structure is shown in Fig. 5(c). Along the symmetry $\boldsymbol{k}$-lines **Γ – M**, **Γ–M'**, **Z – A**, and **Z–A'**, the energy bands of up- and down-spin electrons are split. On the other hand, along the other symmetry $\boldsymbol{k}$-lines and on the symmetry planes **Γ – X – R – Z – Γ** and **X – M – A – R – X**, they are completely the same. Thus, momentum-dependent band spin splitting occurs in the case of β-MnO_2 in a somewhat different way compared to the previous case for α-MnO_2.

In β-MnO_2, both the valence band top (VBT) and the conduction band bottom (CBB) appear with the full spin degeneracy at the **Γ** point. Franchini *et al.*[26] showed a FM ground state of β-MnO_2 with a half-metallic character despite using the same PBE+U calculations with the same value U_{eff} = 4.00 eV as our work. A width of Gaussian smearing is set at 0.01 eV in our calculations, whereas it was set at 0.60 eV in their calculations. Indeed, we also derive the FM ground state instead of the AFM ground state if we increase the smearing to 0.60 eV in our calculation. It suggests that PBE+U calculations with a large smearing width might give misleading information concerning appropriate magnetic order of the manganese-oxide systems.

C. δ-MnO_2

The δ-MnO_2 crystal has a space-group symmetry $P6_3/mmc$ (194) with a hexagonal lattice (HEX, see Fig. 6). The relaxed lattice constants from our geometrical optimization are a = 2.925 Å and c = 11.427 Å, which are somewhat different from the experimental data[51] (a = 2.840 Å and c = 14.031 Å). The discrepancy between experimental and theoretical lattice constants is

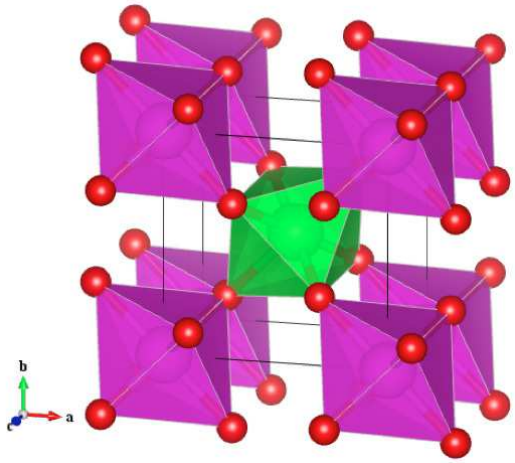

Fig. 4: Primitive unit cell of AFM β-MnO_2.

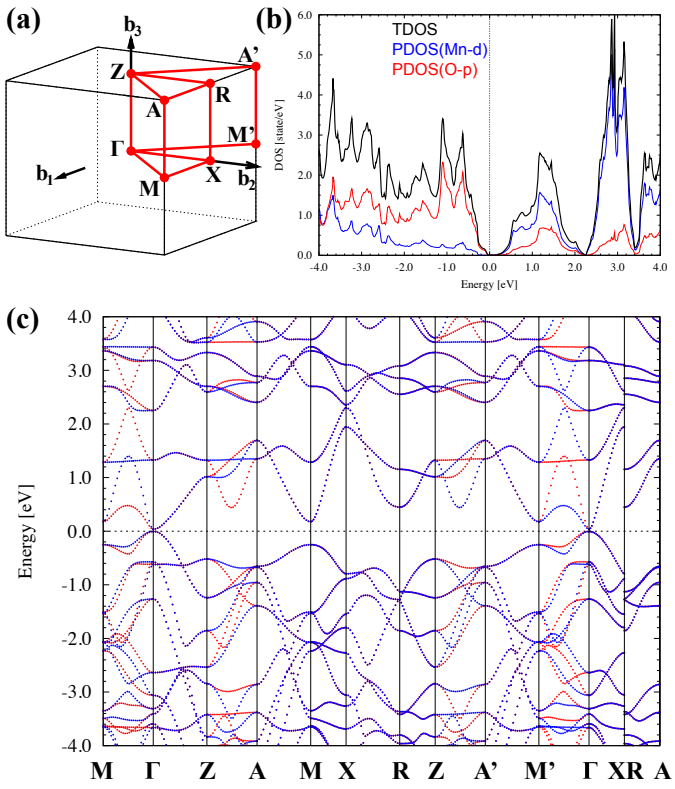

Fig. 5: (a) Brillouin zone of TET lattice for β-MnO_2. The figure is made by slightly modifying Fig. 4 in the reference of AFLOW[40]. (b) Total DOS and partial DOS of manganese 3*d* and oxygen 2*p* orbitals for AFM β-MnO_2. (c) Band structure of AFM β-MnO_2 along the **M–Γ–Z–A–M–X–R–Z–A'–M'–Γ–X | R–A** lines.

due to the fact that the stoichiometric crystal structure is very far from the experimental samples that include potassium atoms and water molecules, *etc*[51]. However, it was confirmed that our result does not change qualitatively even if we use the experimental lattice constants (see Fig. S8 in Supplementary Information). In both FM and AFM cases, each layer has FM ordering because all the oxygen octahedra are connected by ridge sharing [see Figs. 6(a) and (b)]. The calculated energy difference between FM and AFM configurations is almost zero (see Table 1), because the interlayer magnetic interaction is so weak. Therefore, we present band structures of both FM and AFM δ-MnO_2. The Brillouin zone and the DOS in the case of FM configuration are shown in Figs. 7(a) and (b), respectively. In contrast to the two previous cases, the DOS plots for up- and down-spin electrons are separated, although it is the same that the valence and conduction bands are mainly composed of oxygen $2p$ and manganese $3d$ orbitals, respectively. The result indicates that δ-MnO_2 is a semiconductor with a band gap of 1.70 eV. The FM band structure is shown in Fig. 7(c) and the AFM band structures are shown in Figs. 8(a) and (b). Naturally, the FM system reflects that the energy bands of up- and down-spin electrons are different at any $\boldsymbol{k}$-point. In the AFM case, energy bands of up- and down-spin electrons are degenerate at the **Γ** − **M** − **K** − **Γ**, **A** – **L** – **H** – **A**, **Γ** – **K** – **H** – **A** – **Γ**, and **M** – **K** – **H** – **L** – **M** symmetry planes. On the other hand, band spin splitting occurs at the other areas in the Brillouin zone containing also the **Γ** – **M** – **L** – **A** – **Γ** symmetry plane. For example, if we write the middle points of the symmetry line segments **Γ** – **A**, **M** − **L**, and **K** − **H** are **P**, **Q**, and **R**, the **P** − **Q** line is spin split but the **Q** − **R** and **R** − **P** lines are spin degenerate. Moreover, as can be seen in Fig. 8(b), energy levels of up-spin electrons at the **P** – **Q** line are the same as energy levels of down-spin electrons at the **P** – **Q'** line, and *vice versa*, where **Q** and **Q'** points are equivalent with a six-fold rotation C_6 around the c axis.

For this FM δ-MnO_2 phase, we found that the indirect band gap appears between the majority spin (up-spin) states, which is different from the previous result by Kwon *et al.*[27] who suggested the indirect band gap between different spin states. The reason for this difference is presumably due to the absence of the parameter U (*i.e.*, pure GGA) in their calculation. With U_{eff} = 0.00 eV, we also found that the CBB becomes the minority spin (down-spin) state. However, when we set finite value for the Hubbard U, the minority spin state goes up due to the repulsive interaction with the occupied majority spin electron in the manganese $3d$ orbital, and becomes a higher conduction band.

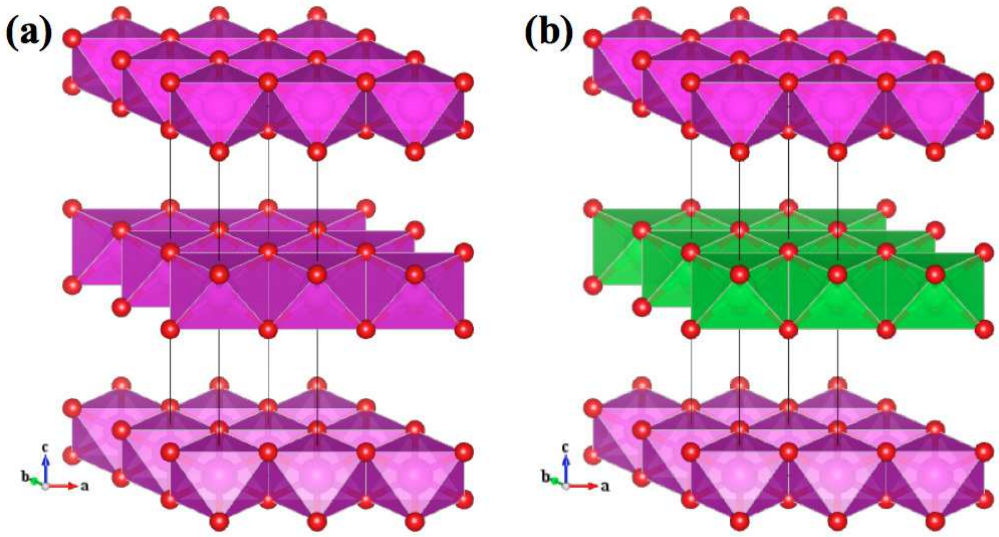

Fig. 6: Primitive unit cells of (a) FM and (b) AFM δ-MnO_2.

D. λ-MnO_2

Unlike the three previous MnO_2 crystals, the definition of spin configuration in λ-MnO_2 is very difficult because there is spin fluctuation in Mn tetrahedron framework[52]. The λ-MnO_2 crystalline phase has a space-group symmetry $Fd\bar{3}m$ (227) with a face-centred cubic (FCC) lattice without consideration of spin configuration. All the oxygen octahedra in the structure of λ-MnO_2 are connected to each other by ridge sharing, and a FM order might be appropriate according to the Goodenough-Kanamori rule for the superexchange interaction. However, it was reported that λ-MnO_2 exhibits an AFM order in the previous experimental study[52]. Following to the reference, we set the AFM order along (111) crystal orientation of λ-MnO_2. Considering to the AFM order, we can set the primitive unit cell having a space-group symmetry $R3m$ (160) with a rhombohedral lattice type 1 (RHL_1, see Fig. 9). The relaxed lattice constants from our geometrical optimization are $a = 10.062$ Å and $\alpha = 33.67°$ (the RHL_1 unit cell with $a = 9.833$ Å and $\alpha = 33.56°$ corresponds to the original FCC unit cell with the experimental lattice constant $a = 8.029$ Å[52]; the corresponding relaxed value is $a = 8.216$ Å). The Brillouin zone and the DOS are shown in Figs. 10(a) and (b), respectively. Again, there is a large contribution of oxygen $2p$ (manganese $3d$) orbitals to the DOS of the valence (conduction) bands. The resulting λ-MnO_2 phase is a semiconductor with an indirect band gap of 1.86 eV [between the **L** point (valence band) and

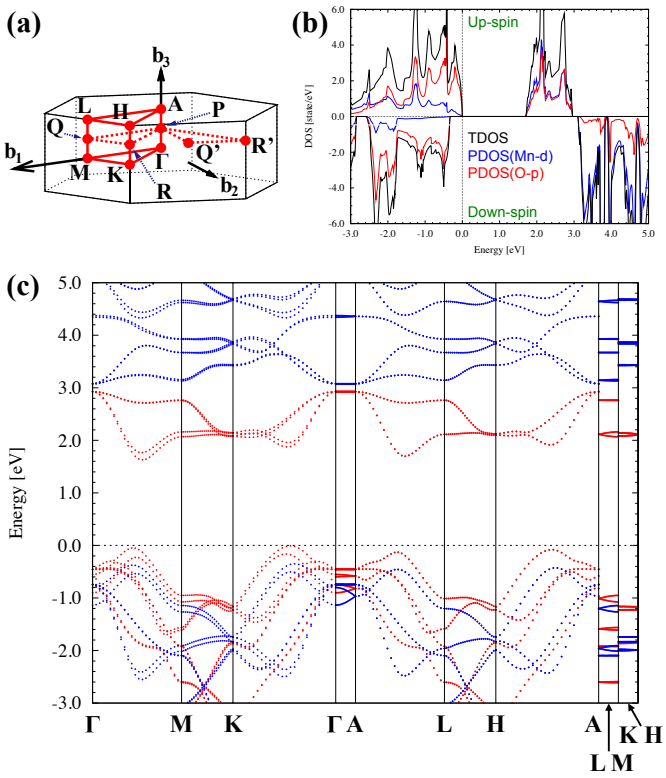

Fig. 7: (a) Brillouin zone of HEX lattice for δ-MnO_2. The figure is made after Fig. 13 in the reference of AFLOW[40]. (b) Total DOS and partial DOS of manganese $3d$ and oxygen $2p$ orbitals for FM δ-MnO_2. Positive and negative values of DOS are for up- and down-spin electrons, respectively. (c) Band structure of FM δ-MnO_2 along the **Γ – M – K – Γ – A – L – H – A | L – M | K – H** lines.

the **P** point (conduction band)]. The band structures of λ-MnO_2 are shown in Figs. 10(c) and (d). Same as AFM δ-MnO_2, there are spin-degenerate band dispersions at any $\boldsymbol{k}$-point. Thus, momentum-dependent band spin splitting does not occur in this case.

IV. DISCUSSION

As we mentioned in Chapter Ⅲ, it is difficult to determine the magnetic interactions of MnO_2 precisely. In spite of the doing it, we estimate penalty energies, which represent the energy enhancement due to the Goodenough-Kanamori rule, *i.e.*, due to the appearance of FM-coupling point sharing and AFM-coupling ridge sharing, E_{P}^{ρ} and E_{R}^{ρ} ($\rho = \alpha$, β, δ, and λ), respectively (the

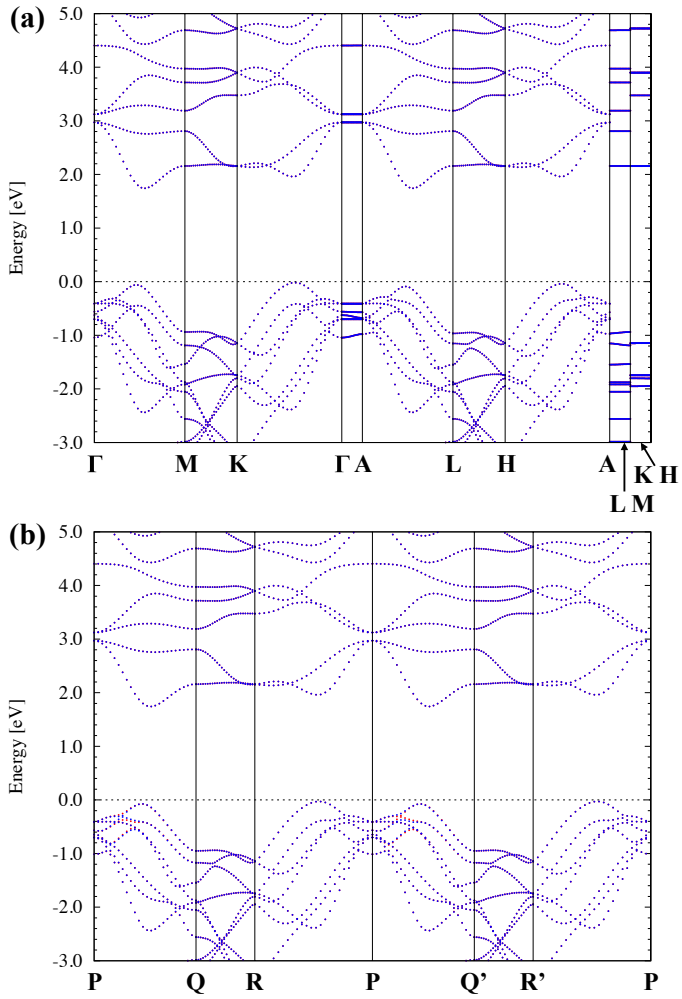

Fig. 8: Band structures of AFM δ-MnO_2 along (a) the **Γ – M – K – Γ – A – L – H – A | L – M | K – H** lines and (b) the **P – Q – R – P–Q'–R'–P** lines.

detail of how to estimate the penalty energies is described in Supplementary Information). From our analysis, we estimate E_P^α = 0.003–0.004 eV and E_R^α = 0.004–0.005 eV for α-MnO_2, E_P^β = 0.003 eV and E_R^β = 0.023 eV for β-MnO_2, E_R^δ = 0.031 eV for δ-MnO_2, and E_R^λ = 0.013–0.019 eV for λ-MnO_2 (see Tables S3 in Supplementary Information). First, we emphasize that E_P^ρ and E_R^ρ are all positive; FM-coupling point sharing and AFM-coupling ridge sharing are energetically unfavourable. In the case of α- and β-MnO_2 having both point and ridge sharings of oxygen octahedra, it is found that E_R^ρ is energetically larger than E_P^ρ. It means that the larger the number of AFM-coupling ridge sharings, the less stable the AFM MnO_2 system, independent of the number

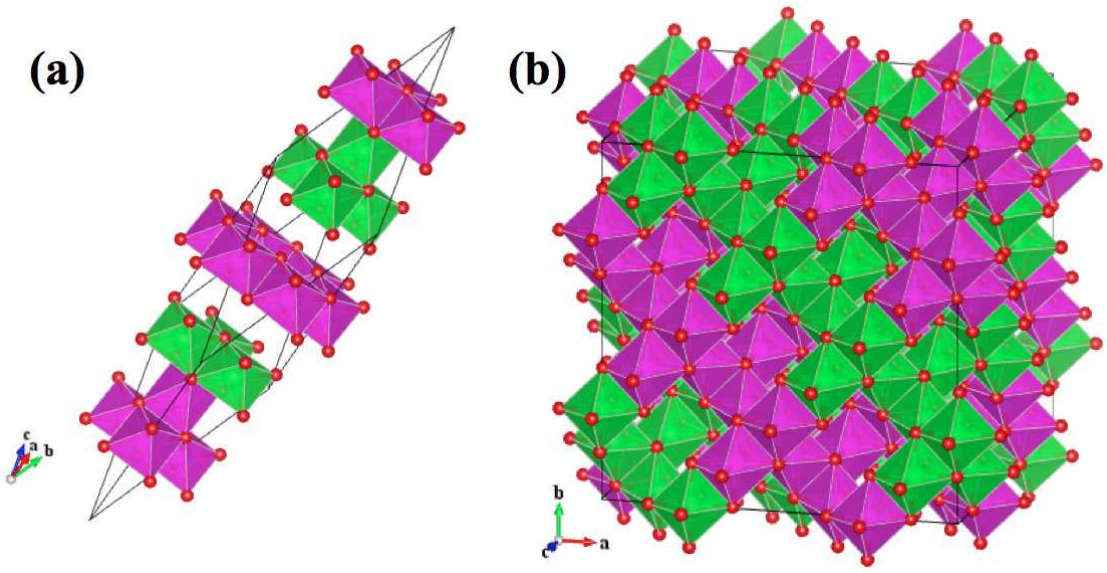

Fig. 9: (a) Primitive and (b) conventional unit cells of AFM λ-MnO_2.

of FM-coupling point sharings.

The results of spin splitting and degeneracy for all the MnO_2 structures studied in this paper are briefly summarized as follows. In the case of AFM α-, β-, and δ-MnO_2, up- and down-spin band dispersions fully coincide along some symmetry $\boldsymbol{k}$-lines (and on some symmetry $\boldsymbol{k}$-planes for β- and δ-MnO_2), while they are splitting at the other $\boldsymbol{k}$-points. In the case of FM δ-MnO_2, up- and down-spin bands are completely different at any $\boldsymbol{k}$-point. In the case of AFM λ-MnO_2, they are fully degenerate at any $\boldsymbol{k}$-point. Regarding the relationship between geometrical structures and band dispersions, we found that the orientation of oxygen octahedra in each AFM MnO_2 crystal is very crucial to understand whether up- and down-spin energy bands split or degenerate in the AFM MnO_2 crystals. It is essentially related to the fact that the effective single-electron potential (or the nuclear potential plus the self-energy) V_σ ($\sigma =\uparrow$ or $\downarrow$) is spin dependent in the Kohn-Sham (or quasiparticle) equations

$$\left[\frac{1}{2}(\boldsymbol{k} - i\nabla)^2 + V_\uparrow\right]u_{k\uparrow} = \epsilon_{k\uparrow}u_{k\uparrow}, \tag{1a}$$

$$\left[\frac{1}{2}(\boldsymbol{k} - i\nabla)^2 + V_\downarrow\right]u_{k\downarrow} = \epsilon_{k\downarrow}u_{k\downarrow}, \tag{1b}$$

for up-spin (Eq. 1a) and down-spin (Eq. 1b) electrons, where $\epsilon_{k\sigma}$ and $u_{k\sigma}$ denote the eigenvalue and the periodic eigenfunction at each $\boldsymbol{k}$-point, respectively.

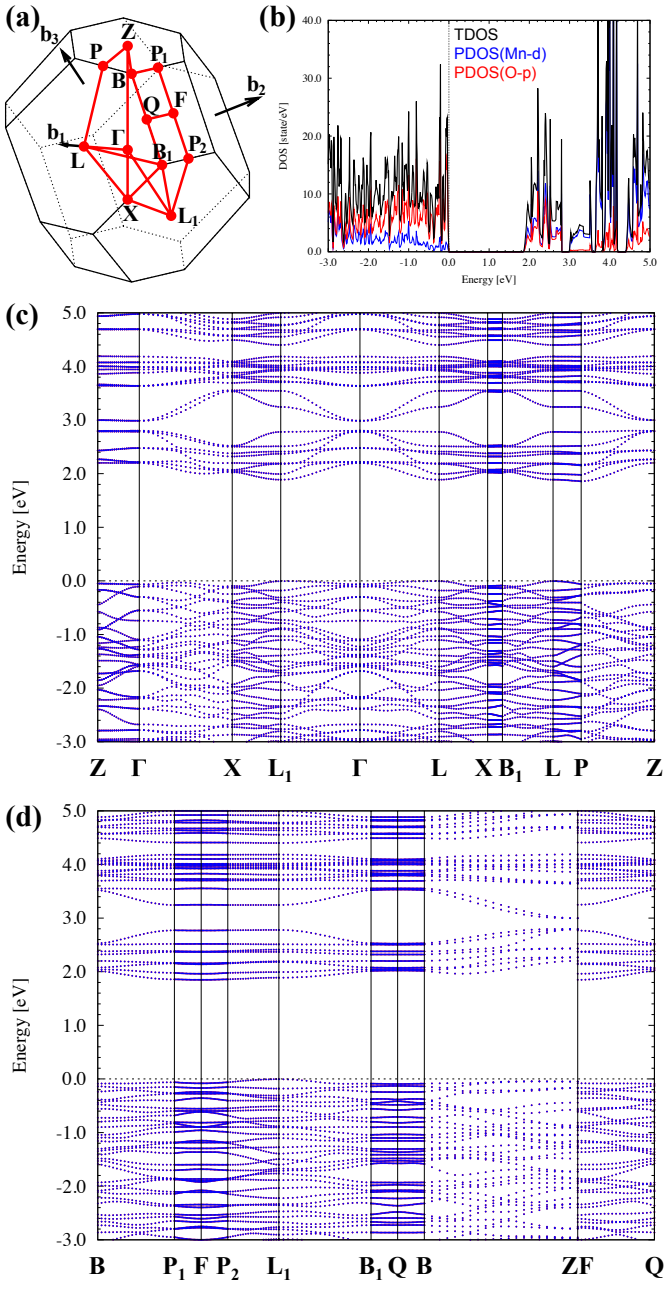

Fig. 10: (a) Brillouin zone of RHL_1 lattice for λ-MnO_2. The figure is made by modifying Fig. 14 in the reference of AFLOW[40]. (b) Total DOS and partial DOS of manganese 3*d* and oxygen 2*p* orbitals for AFM λ-MnO_2. Band structures of AFM λ-MnO_2 along (c) the **Z – Γ – X – L_1 – Γ – L – X – B_1 – L – P – Z** lines and (d) the **B – P_1 – F – P_2 – L_1 – B_1 – Q – B – Z | F – Q** lines.

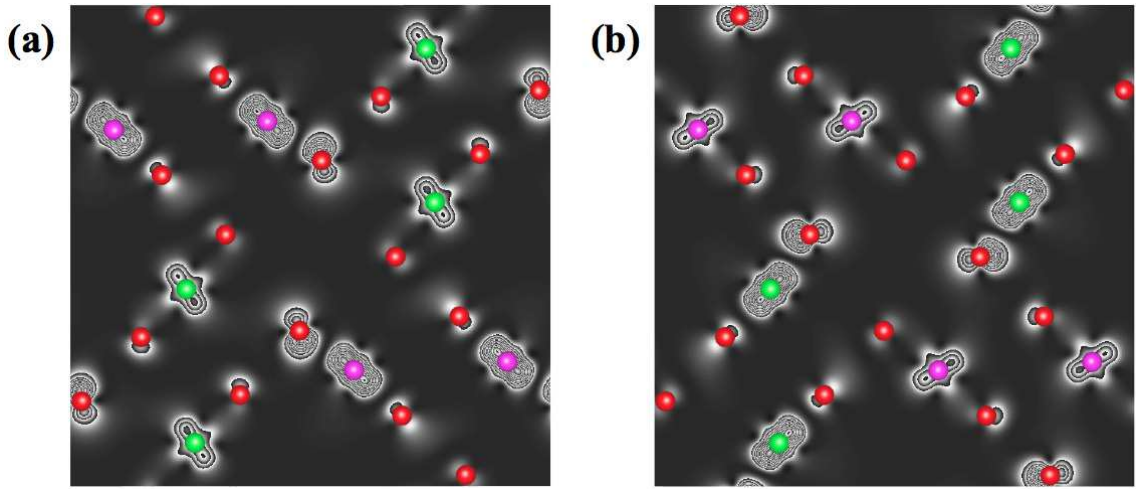

Fig. 11: The PDDs of the CBB of (a) up-spin density at the **X** point and (b) down-spin density at the **X'** point for α-MnO_2. They can be seen from a direction along the c axis of the tetragonal supercell showed in Fig. 2(b).

Suppose a space-group symmetry operation $\mathcal{R}$ that maps the magenta-coloured (up-spin) octahedra onto the green-coloured (down-spin) octahedra, *i.e.*, it satisfies $\mathcal{R}V_\sigma = V_{-\sigma}$. For example, consider a four-fold rotation C_4 around the c axis of α-MnO_2; see Fig. 2(b). It maps the magenta-coloured octahedra onto the green-coloured octahedra. In the case of β-MnO_2 (see Fig. 4), there are a four-fold rotation C_4 around the c axis and two-fold rotations C_2 around the a and b axes both of which follow glide-plane $(1/2)$ translation. For δ-MnO_2, a horizontal reflection $\mathcal{M}_h$ perpendicular to the c axis and a combination of a vertical reflection $\mathcal{M}_v$ parallel to the c axis and a six-fold rotation C_6 around the c axis (namely, $\mathcal{M}_vC_6$) are important [see Fig. 6(b)]. In this case, they satisfy $\mathcal{M}_hV_\sigma = V_{-\sigma}$ and $\mathcal{M}_vC_6V_\sigma = V_{-\sigma}$, respectively. For λ-MnO_2, the magenta-coloured octahedra map onto the green-coloured octahedra under a translation $\mathcal{T}$, so that we have $\mathcal{T}V_\sigma = V_{-\sigma}$, because all the orientation of the oxygen octahedra are the same regardless of their spin configurations; see Figs. 9(a) and (b). All these operations as well as their alternatives $\mathcal{I}C_n$ ($n = 2$ or 4) combined with the inversion operation $\mathcal{I}$ satisfy $\mathcal{R}V_\sigma = V_{-\sigma}$. Now, if a certain wave vector $\boldsymbol{k}$ is unchanged under at least one of these space-group operations $\mathcal{R}$, *i.e.*, satisfies $\mathcal{R}\boldsymbol{k} = \boldsymbol{k}$, the square parenthesis of the left hand side of Eq. (1a) under this operation becomes identical to that of Eq. (1b), and *vice versa*. That is, for such wave vector $\boldsymbol{k}$, Eqs. (1a) and (1b) become identical to each other, and we find the spin degeneracy: $\epsilon_{k\uparrow} = \epsilon_{k\downarrow}$. For example, the $\mathbf{\Gamma} - \mathbf{Z}$ line continuing to the

$\mathbf{Z_1} - \mathbf{M}$ line in α-MnO_2 [see Fig. 3(a)] is spin degenerate because we have $C_4\boldsymbol{k} = \boldsymbol{k}$ for any $\boldsymbol{k}$ vector along this line. Similarly, the $\mathbf{\Gamma} - \mathbf{X} - \mathbf{R} - \mathbf{Z} - \mathbf{\Gamma}$ and $\mathbf{X} - \mathbf{M} - \mathbf{A} - \mathbf{R} - \mathbf{X}$ planes in β-MnO_2 [see Fig. 5(a)] are spin degenerate because we have $\mathcal{I}C_2\boldsymbol{k} = \boldsymbol{k}$ or $\mathcal{I}C_2\boldsymbol{k} = \boldsymbol{k} - \boldsymbol{G}$, where $\boldsymbol{G}$ is a reciprocal lattice vector. In the case of δ-MnO_2, the $\mathbf{\Gamma} - \mathbf{M} - \mathbf{K} - \mathbf{\Gamma}$ and $\mathbf{A} - \mathbf{L} - \mathbf{H} - \mathbf{A}$ planes are spin degenerate because $\mathcal{M}_h\boldsymbol{k} = \boldsymbol{k}$ or $\mathcal{M}_h\boldsymbol{k} = \boldsymbol{k} - \boldsymbol{b}_3$ is satisfied. In addition, the $\mathbf{\Gamma} - \mathbf{K} - \mathbf{H} - \mathbf{A} - \mathbf{\Gamma}$ and $\mathbf{M} - \mathbf{K} - \mathbf{H} - \mathbf{L} - \mathbf{M}$ planes are spin degenerate because $\mathcal{M}_v C_6\boldsymbol{k} = \boldsymbol{k}$ or $\mathcal{M}_v C_6\boldsymbol{k} = \boldsymbol{k} - \boldsymbol{G}$ is satisfied. Moreover, λ-MnO_2 is fully spin degenerate for arbitrary $\boldsymbol{k}$-points because $\mathcal{T}\boldsymbol{k} = \boldsymbol{k}$. Using a similar argument, we can also derive $\epsilon_{\boldsymbol{k}\uparrow} = \epsilon_{\boldsymbol{k}'\downarrow}$ for two different wave vectors $\boldsymbol{k}$ and $\boldsymbol{k}'$ that are related to each other by $\mathcal{R}\boldsymbol{k} = \boldsymbol{k}'$. Indeed, the up- and down-spin energy bands on the $\mathbf{\Gamma} - \mathbf{M}$ and **Γ–M'** lines in α- and β-MnO_2 [see Figs. 3(c) and 5(c)] are identical if we change $\uparrow$ and $\downarrow$. Similarly, the $\mathbf{\Gamma} - \mathbf{X}$ and **Γ–X'** lines in α-MnO_2 are also related to each other in this manner. Figures 11(a) and (b) represent, the up-spin partial density distribution (PDD) at the **X** point and the down-spin PDD at the **X'** point of α-MnO_2. It is readily seen from these figures that the up-spin PDD at the **X** point precisely coincides with the down-spin PDD at the **X'** point when we rotate the system by 90° around the c axis. Such spin degeneracies exist in these crystalline phases. However, for general wave vectors $\boldsymbol{k}$ that do not satisfy $\mathcal{R}\boldsymbol{k} = \boldsymbol{k}$, we have spin splitting $\epsilon_{\boldsymbol{k}\uparrow} \neq \epsilon_{\boldsymbol{k}'\downarrow}$.

In this manner, different orientations of oxygen octahedra in the AFM α-, β-, and δ-MnO_2 crystals can keep spin degeneracy only at some symmetry $\boldsymbol{k}$-lines or planes due to some space-group symmetries, but the same orientations of oxygen octahedra in the AFM λ-MnO_2 crystal can keep spin degeneracy at any $\boldsymbol{k}$-point inside the whole Brillouin zone due to the translational symmetry.

It indicates that there is no spin degeneracy in the vicinity of the VBT and the CBB for AFM α- and β-MnO_2 even though the VBT and the CBB themselves are the symmetry points (the **M**, **M'**, **X**, and **X'** points for α-MnO_2 or the **Γ** point for β-MnO_2) and spin degenerate. In contrast, there are spin degeneracies in the vicinity of the VBT and the CBB for AFM λ-MnO_2 because this phase has the full spin degeneracy. Since the electronic states in the vicinity of the VBT and the CBB should have major contribution to any kind of catalytic reactions, we speculate that AFM λ-MnO_2 can be a more efficient catalyst in a sense that both up- and down-spin electrons can contribute to the same chemical reaction. Indeed, it has been recently observed that the oxygen-evolution rate is the highest in λ-MnO_2 compared to the other crystal phases of MnO_2[18,19]. Whereas, in the case of AFM α- and β-MnO_2, it is expected that a catalytic reaction depending on the electron-

momentum and spin orientations may take place because only up- or down-spin band exist in the vicinity of VBT and CBB according to the electron momentum [*e.g.*, around the **X** and **X'** points (along the **Γ−M** and **Γ−M'** lines) in the Brillouin zone of α-MnO_2 (β-MnO_2)]. However the meaning of this catalytic reaction depending on the directions of the electron-momentum and the spin orientation is still abstract, and it is required to further explore its real physical meaning and possible applications in the future.

V. CONCLUSION

We have presented a comprehensive study of stoichiometric α-, β-, δ-, and λ-MnO_2 crystals using spin-polarized DFT with PAW and PBE+U. Due to the lack of accurate experimental and theoretical information on the pristine MnO_2 crystals, it is not easy to judge which magnetic order is the most appropriate. Nevertheless, we have estimated the penalty energies in order to reveal the origin of the magnetic energy difference between the different FM and AFM configurations of the MnO_2 crystals. It is found that superexchange interactions of Mn–O–Mn groups dominate the magnetic interactions in the MnO_2 crystals. According to our analysis, we have determined the magnetic configurations of the pristine MnO_2 crystals with focusing on each spin orientation of Mn atoms. Based on some references on electronic states and magnetic behaviours of the MnO_2 crystals, we have selected the most probable magnetic orders of the MnO_2 and discussed their momentum-dependent band spin splitting.

In the case of FM MnO_2 (the layered δ-MnO_2 in this study), majority- and minority-spin band dispersions exhibit different energy levels at all $\boldsymbol{k}$-points in the band structure shown in Fig. 7(c). The synthesized δ-MnO_2 crystals in experimental references are non-stoichiometric compounds containing some alkali metals, alkaline earth metals, water molecules, and/or oxygen vacancies[51,53–57]. Our results would give a good starting point in discussing the accurate electronic states of such imperfect δ-MnO_2 in a future work on artificial photosynthesis. In contrast, AFM orders are investigated for all of the four different MnO_2 crystals. Looking at their band structures in Figs. 3(c) and (d) of α-MnO_2, Fig. 5(c) of β-MnO_2, and Fig. 8(b) of δ-MnO_2, there are spin-split band dispersions at some symmetry $\boldsymbol{k}$-lines or planes. However, there is no spin-split band dispersion in the band structures in Figs. 10(c) and (d) of λ-MnO_2. We find that such unique momentum-dependent band spin splitting and degeneracy are related to the orientation in the AFM MnO_2 crystals of Mn-centred oxygen octahedra.

The most important point in these crystals is that there is a symmetry operation $\mathcal{R}$ that maps all up-spin Mn-centred oxygen octahedra onto all down-spin Mn-centred oxygen octahedra (*i.e.*, $\mathcal{R}V_\sigma = V_{-\sigma}$ is satisfied). For any wave vector $\boldsymbol{k}$ that satisfies $\mathcal{R}\boldsymbol{k} = \boldsymbol{k}$, we have spin degeneracy. For two different wave vectors $\boldsymbol{k}$ and $\boldsymbol{k}'$ that satisfy $\mathcal{R}\boldsymbol{k} = \boldsymbol{k}'$, the up-spin bands at $\boldsymbol{k}$ coincides with the down-spin bands at $\boldsymbol{k}'$, and *vice versa*. These facts provide a better understanding for the accurate spin states of AFM materials. Recently, spin-split band dispersions have attracted much attention in the context of topological insulators. In the present case, we can find the spin-split band structures even in ordinary three-dimensional systems without the spin-orbit coupling or the breaking of the time-reversal symmetry. The mechanism is independent of the time-reversal symmetry. In our case, the difference in the symmetry on particular axes (*e.g.*, rotational symmetry on the *c* axis and no rotational symmetry on the *a* and *b* axes in the α-MnO_2) leads to the momentum-dependent band spin splitting or degeneracy.

If we compare the present results with the experimental measurements on the reaction rate of the photochemical oxygen evolution of various MnO_2 phases by Dismukes' group[18,19], our results seem to be consistent with their experimental findings that AFM λ-MnO_2 has the largest reaction rate in a sense that both up- and down-spin electrons in the vicinity of the VBT and the CBB can equally contribute to the oxygen-evolution reaction. However, further discussion concerning the relationship to the catalytic behaviour is needed and left for the future study.

Acknowledgments

This work is supported by Grant-in-Aid for Science Research B (Grant No. 25289218) from Japan Society for the Promotion of Science (JSPS). We have been also indebted to High Performance Computer Infrastructure (HPCI) and Computational Materials Science Initiative (CMSI) both promoted by Ministry of Education, Culture, Sports, Science and Technology (MEXT) of Japan for the use of a supercomputer SR16000 at Hokkaido University Computing Center (HUCC), Hokkaido University and Institute for Materials Research (IMR), Tohoku University (Project IDs. hp140214 and hp150231).

* yusuke.noda@riken.jp

[1] J. E. Post, *Proc. Natl. Acad. Sci.*, 1999, **96**, 3447.

[2] B. Ammundsen and J. Paulsen, *Adv. Mater.*, 2001, **13**, 943.

[3] M. M. Tackeray, S.-H. Kang, C. S. Johnson, J. T. Vaughey, R. Benedek and S. A. Hackney, *J. Mater. Chem.*, 2007, **17**, 3112.

[4] T. Kim, E. Momin, J. Choi, K. Yuan, H. Zaidi, J. Kim, M. Park, N. Lee, M. T. McMahon, A. Quinones-Hinojosa, J. W. M. Bulte, T. Hyeon and A. A. Gilad, *J. Am. Chem. Soc.*, 2011, **133**, 2955.

[5] Z.-R. Tian, W. Tong, J.-Y. Wang, N.-G. Duan, V. V. Krishnan and S. L. Suib, *Science*, 1997, **276**, 926.

[6] L. Mao, D. Zhang, T. Sotomura, K. Nakatsu, N. Koshiba and T. Ohsaka, *Electro. Acta*, 2003, **48**, 1015.

[7] J. Yano and V. Yachandra, *Chem. Rev.*, 2014, **114**, 4175.

[8] Y. Umena, K. Kawakami, J.-R. Shen and N. Kamiya, *Nature*, 2011, **473**, 55.

[9] M. Suga, F. Akita, K. Hirata, G. Ueno, H. Murakami, Y. Nakajima, T. Shimizu, K. Yamashita, M. Yamamoto, H. Ago and J.-R. Shen, *Nature*, 2015, **517**, 99.

[10] N. Cox, M. Retegan, F. Neese, D. A. Pantazis, A. Boussac and W. Lubitz, *Science*, 2014, **345**, 6198.

[11] D. A. Pantazis, W. Ames, N. Cox, W. Lubitz and F. Neese, *Angew. Chem. Int. Ed.*, 2012, **51**, 9935.

[12] P. E. M. Siegbahn, *J. Am. Chem. Soc.*, 2013, **135**, 9442.

[13] K. Saito and H. Ishikita, *Biochem. Biophys. Acta*, 2014, **1837**, 159.

[14] J. Yang, M. Hatakeyama, K. Ogata, S. Nakamura and C. Li, *J. Phys. Chem. B*, 2014, **118**, 14215.

[15] B. Kok, B. Forbush and M. McGloin, *Photochem. Photobiol.*, 1970, **11**, 457.

[16] J. Turner, *Nat. Mater.*, 2008, **7**, 770.

[17] T. Reier, M. Oezaslan and P. Strasser, *ACS Catal.*, 2012, **2**, 1765.

[18] D. M. Robinson, Y. B. Go, M. Greenblatt and G. C. Dismukes, *J. Am. Chem. Soc.*, 2010, **132**, 11467.

[19] D. M. Robinson, Y. B. Go, M. Mui, G. Gardner, Z. Zhang, D. Mastrogiovanni, E. Garfunkel, J. Li, M. Greenblatt and G. C. Dismukes, *J. Am. Chem. Soc.*, 2013, **135**, 3494.

[20] M. Huynh, D. K. Bediako and D. G. Nocera, *J. Am. Chem. Soc.*, 2014, **136**, 6002.

[21] C.-H. Kuo, I. M. Mosa, A. S. Poyraz, S. Biswas, A. M. El-Sawy, W. Song, Z. Luo, S.-Y. Chen, J. F. Rusling, J. He and S. L. Suib, *ACS Catal.*, 2015, **5**, 1693.

[22] M. M. Najafpour, T. Ehrenberg, M. Wiechen and P. Kurz, *Angew. Chem. Int . Ed.*, 2010, **49**, 2233.

[23] M. Wiechen, I. Zaharieva, H. Dau and P. Kurz, *Chem. Sci.*, 2012, **3**, 2330.

[24] C. E. Frey, M. Wiechen and P. Kurz, *Dalton Trans.*, 2014, **43**, 4370.

[25] E. Cockayne and L. Li, *Chem. Phys. Lett.*, 2012, **544**, 53.

[26] C. Franchini, R. Podloucky, J. Paier, M. Marsman and G. Kresse, *Phys. Rev. B*, 2007, **75**, 195128.

[27] K. D. Kwon, K. Refson and G. Sposito, *Phys. Rev. Lett.*, 2008, **100**, 146601.

[28] C. Sun, Y. Wang, J. Zou and S. C. Smith, *Phys. Chem. Chem. Phys.*, 2011, **13**, 11325.

[29] D. Morgan, B. Wang, G. Ceder and A. van de Walle, *Phys. Rev. B*, 2003, **67**, 134404.

[30] C. L. Kane and E. J. Mele, *Phys. Rev. Lett.*, 2005, **95**, 146802.

[31] L. Fu and C. L. Kane, *Phys. Rev. B*, 2007, **76**, 045302.

[32] G. Kresse and J. Furthmüller, *Phys. Rev. B*, 1996, **54**, 11169.

[33] P. E. Blöchl, *Phys. Rev. B*, 1994, **50**, 17953.

[34] G. Kresse and D. Joubert, *Phys. Rev. B*, 1999, **59**, 1758.

[35] J. P. Perdew, K. Burke and M. Ernzerhof, *Phys. Rev. Lett.*, 1996, **77**, 3865.

[36] S. L. Dudarev, G. A. Botton, S. Y. Savrasov, C. J. Humphreys and A. P. Sutton, *Phys. Rev. B*, 1998, **57**, 1505.

[37] H. J. Monkhorst and J. D. Pack, *Phys. Rev. B*, 1976, **13**, 5188.

[38] P.E. Blöchl, O. Jepsen and O.K. Andersen, *Phys. Rev. B*, 1994, **49**, 16223.

[39] A. Togo and I. Tanaka, *Phys. Rev. B*, 2013, **87**, 184104.

[40] W. Setyawan and S. Curtarolo, *Comput. Mater. Sci.*, 2010, **49**, 299.

[41] S. Curtarolo, W. Setyawan, G. L. W. Hart, M. Jahnatek, R. V. Chepulskii, R. H. Taylor, S. Wang, J. Xue, K. Yang, O. Levy, M. J. Mehl, H. T. Stokes, D. O. Demchenko and D. Morgan *Comput. Mater. Sci.*, 2012, **58**, 218.

[42] J. B. Goodenough, *Phys. Rev.*, 1955, **100**, 564.

[43] J. Kanamori, *J. Phys. Chem. Sol.*, 1959, **10**, 87.

[44] P. A. Cox, *Transition Metal Oxides: An Introduction to Their Electronic Structure and Properties*, Clarendon Press, Oxford, 1995.

[45] P. J. Hay, J. C. Thibeault, and R. Hoffmann, *J. Am. Chem. Soc.*, 1975, **97**, 4884.

[46] H. Xiang, C. Lee, H.-J. Koo, X. Gonga, and M.-H. Whangbo, *Dalton Trans.*, 2013, **42**, 823.

[47] V. I. Anisimov, F. Aryasetiawan, and A. I. Lichtenstein, *J. Phys.: Condens. Matter*, 1997, **9**, 767.

[48] R. M. Martin, *Electronic Structure: Basic Theory and Practical Methods*, Cambridge University Press, New York, 2004.

[49] C. S. Johnson, D. W. Dees, M. F. Mansuetto, M. M. Thackeray, D. R. Vissers, D. Argyriou, C.-K. Loong and L. Christenen, *J. Pow. Sour.*, 1997, **68**, 570.

[50] A. A. Bolzan, C. Fong, B. J. Kennedy and C. J. Howard, *Aust. J. Chem.*, 1993, **46**, 939.

[51] A.-C. Gaillot, D. Flot, V. A. Drits, A. Manceau, M. Burghammer and B. Lanson, *Chem. Mater.*, 2003, **15**, 4666.

[52] J. E. Greedan, N. P. Raju, A. S. Wills, C. Morin, S. M. Shaw and J. N. Reimers, *Chem. Mater.*, 1998, **10**, 3058.

[53] J. E. Post and D. R. Veblen, *Am. Min.*, 1990, **75**, 477.

[54] A. Ertl, F. Pertlik, M. Prem, J. E. Post, S. J. Kim, F. Brandstätter, and R. Schuster, *Eur. J. Mineral.*, 2005, **17**, 163.

[55] T. Takashima, K. Hashimoto and R. Nakamura, *J. Am. Chem. Soc.*, 2012, **134**, 1519.

[56] T. Takashima, K. Hashimoto and R. Nakamura, *J. Am. Chem. Soc.*, 2012, **134**, 18153.

[57] F. F. Marafatto, M. L. Strader, J. Gonzalez-Holguera, A. Schwartzberg, B. Gilbert and J. Peña, *Proc. Natl. Acad. Sci.*, 2015, **112**, 4600.